A forward model and conjugate gradient inversion technique for low-frequency ultrasonic imaging

Koen W. A. van Dongen[a] and William M. D. Wright[b]
Ultrasonics Research Group, Department of Electrical and Electronic Engineering, University College Cork, College Road, Cork, Ireland

(Received 31 August 2005; revised 19 July 2006; accepted 20 July 2006)

Emerging methods of hyperthermia cancer treatment require noninvasive temperature monitoring, and ultrasonic techniques show promise in this regard. Various tomographic algorithms are available that reconstruct sound speed or contrast profiles, which can be related to temperature distribution. The requirement of a high enough frequency for adequate spatial resolution and a low enough frequency for adequate tissue penetration is a difficult compromise. In this study, the feasibility of using low frequency ultrasound for imaging and temperature monitoring was investigated. The transient probing wave field had a bandwidth spanning the frequency range 2.5–320.5 kHz. The results from a forward model which computed the propagation and scattering of low-frequency acoustic pressure and velocity wave fields were used to compare three imaging methods formulated within the Born approximation, representing two main types of reconstruction. The first uses Fourier techniques to reconstruct sound-speed profiles from projection or Radon data based on optical ray theory, seen as an asymptotical limit for comparison. The second uses backpropagation and conjugate gradient inversion methods based on acoustical wave theory. The results show that the accuracy in localization was 2.5 mm or better when using low frequencies and the conjugate gradient inversion scheme, which could be used for temperature monitoring. © *2006 Acoustical Society of America.* [DOI: 10.1121/1.2336752]

PACS number(s): 43.60.Pt, 43.20.Dk, 43.20.El, 43.80.Qf, 43.60.Uv [TDM] Pages: 2086–2095

I. INTRODUCTION

Ultrasonic tomographic imaging[1–3] is a well-established technique for medical diagnosis, with the majority of ultrasonic imaging systems relying on backscattered ultrasonic energy to produce an image. There has long been an interest in using ultrasound for the imaging of temperature distributions in the human body (e.g., Johnson *et al.*[4]), particularly during high temperature hyperthermia cancer treatments such as high intensity focused ultrasound (HIFU).[5,6] During this treatment, necrosis of cancer cells is obtained by increasing the tumor temperature to 50–55 °C for a duration of 1 or 2 min or over a shorter period of time for temperatures over 60 °C.[7,8] For successful treatment, it is important that the tumor temperature is sufficiently high to induce necrosis while the normal tissue surrounding the tumor remains at or near normal body temperature to prevent excessive damage. The noninvasive nature of this method results in a lack of direct visual control and therefore requires a monitoring system. Ultrasound as a guidance method has the advantages of being relatively cheap and compatible with HIFU apparatus.

Several methods of ultrasonic estimation of temperature using backscattered ultrasound have been devised, with the majority of techniques based on the observation that biological tissues can be described by semiregular lattices of which the scattering properties change as a function of temperature[9–13] and others based on thermally induced strain.[14–16] As the acoustic contrast between many different soft tissues (or between regions of the same tissue at different temperatures) is relatively small, using backscattered ultrasound to provide the necessary quantitative information for clinical diagnosis or temperature estimation is often difficult. Under these circumstances, other imaging methods utilizing through-transmission may be more appropriate,[17] which have also been used for temperature estimation.[18,19]

Such imaging techniques typically require a compromise between using a high enough frequency for adequate spatial resolution, and a low enough frequency for adequate tissue penetration. It would seem, therefore, that certain benefits could be obtained by imaging at low frequencies, and this has been used with some success for strongly reflective or scattering media such as bone,[20,21] and other applications.[22] The focus of the current study is to use simulation to assess the feasibility of using low frequency (2.5–320 kHz) and therefore highly penetrating ultrasound to image the weakly scattering contrasts expected during HIFU treatment, where a change in temperature from 37 to 50 °C typically produces a contrast in sound speed of only 6 m/s.[23,14,15]

The various imaging methods using diagnostic ultrasound that have been investigated previously are based on different approximations and are consequently not usually compared directly with each other. Common assumptions are that the Born approximation holds, and that only backscattered ultrasound is considered, as this greatly simplifies the mathematics of the inverse scattering problem,[1] a topic still under much scrutiny.[24] In this study, both the transmitted and the backscattered ultrasound are considered together in a full solution. Two types of methods that could be used for measuring the temperature distributions or contrast functions in

[a]Electronic mail: koen@rennes.ucc.ie
[b]Electronic mail: bill.wright@ucc.ie

and around the tumor with low-frequency ultrasound are compared using simulation. The first is computed tomography[25] and is based on optical ray theory. Here, filtered backprojection, Fourier techniques, or algebraic reconstruction techniques are used to relate projection data, i.e., time delays obtained via tomographic measurements, to temperature distributions.[18,26] Good comparisons between the methods within this group have been published by Nawata[18] and Kak *et al.*[25] Despite the obvious disadvantages of using straight ray or simple diffraction assumptions, the major advantage of these techniques is that they require little processing and therefore are fast and easy to implement. As such, there are still many practical applications and recently a system was proposed where these methods will be used for early breast cancer diagnosis.[27] However, most of these techniques require large data sets and tend to neglect the combined effects of diffraction, attenuation, and multiple scattering. As a representative method from this group of techniques, the Fourier slice technique[25,28] has been selected for comparison in this study.

The second group of imaging methods uses acoustical wave theory as the starting point for which various inversion methods have been developed.[29] Here, backpropagation and a conjugate gradient iterative inversion scheme[30,31] have been chosen as representative examples.

Testing of the imaging algorithms is done using synthetic data. These data are obtained by solving the forward (scattering) problem for known contrast functions representing regions positioned in a homogeneous background medium. In some applications, the approach for solving the forward problem is to neglect effects like diffraction and to use far field or Born approximations as done, e.g., in Refs. 32 and 36. However, in the past few years, various methods have been developed to compute synthetic data which take these effects into account, e.g., by using finite element techniques,[33] finite difference time domain techniques,[34] or by solving the representative integral equations via conjugate gradient (CG) inversion schemes.[35–37] In this study, the conjugate gradient technique is used to solve the forward problem in the temporal Laplace domain. In this way, the same computational scheme is used for both the forward problem and the imaging. Fourier transformations are used to obtain synthetic time domain data.

II. FORWARD PROBLEM

The forward problem is solved in the temporal Laplace domain with Laplace parameter $\hat{s}$. Hence, frequency domain results are obtained by taking the limit $\hat{s} \rightarrow -i\omega$, with $i^2 = -1$ and ω the temporal angular frequency. The caret symbol is used to show the frequency dependence of a parameter. In addition, a position in the spatial domain $\mathbb{R}^3$ is notated by the vector $\mathbf{x}$.

By applying reciprocity[38] on the acoustic wave field equations it can be shown that the total pressure wave field $\hat{p}^{\text{tot}}(\mathbf{x})$ and the total velocity wave fields $\hat{v}_k^{\text{tot}}(\mathbf{x})$ and $\hat{v}_j^{\text{tot}}(\mathbf{x})$ for $\{k,j\} = 1$, 2, or 3 equals

$$\hat{p}^{\text{tot}}(\mathbf{x}) = \hat{p}^{\text{inc}}(\mathbf{x}) + \hat{p}^{\text{sct}}(\mathbf{x}), \tag{1}$$

$$\hat{v}_k^{\text{tot}}(\mathbf{x}) = \hat{v}_k^{\text{inc}}(\mathbf{x}) + \hat{v}_k^{\text{sct}}(\mathbf{x}), \tag{2}$$

where $\hat{p}^{\text{inc}}(\mathbf{x})$ and $\hat{v}_k^{\text{inc}}(\mathbf{x})$ are the incident pressure and velocity fields and where $\hat{p}^{\text{sct}}(\mathbf{x})$ and $\hat{v}_k^{\text{sct}}(\mathbf{x})$ refer to the scattered pressure and velocity fields. In the presence of objects represented by contrasts in the acoustic medium parameters compressibility κ and volume density of mass ρ, these scattered wave fields are equal to

$$\hat{p}^{\text{sct}}(\mathbf{x}) = \hat{G}^{pq}(\mathbf{x},\mathbf{x}')[\Delta\hat{\eta}(\mathbf{x}')\hat{p}^{\text{tot}}(\mathbf{x}')] + \sum_{j=1}^{3} \hat{G}_j^{pf}(\mathbf{x},\mathbf{x}') \times [\Delta\hat{\zeta}(\mathbf{x}')\hat{v}_j^{\text{tot}}(\mathbf{x}')], \tag{3}$$

$$\hat{v}_k^{\text{sct}}(\mathbf{x}) = \hat{G}_k^{vq}(\mathbf{x},\mathbf{x}')[\Delta\hat{\eta}(\mathbf{x}')\hat{p}^{\text{tot}}(\mathbf{x}')] + \sum_{j=1}^{3} \hat{G}_{k,j}^{vf}(\mathbf{x},\mathbf{x}') \times [\Delta\hat{\zeta}(\mathbf{x}')\hat{v}_j^{\text{tot}}(\mathbf{x}')], \tag{4}$$

where the contrasts $\Delta\hat{\eta}(\mathbf{x})$ and $\Delta\hat{\zeta}(\mathbf{x})$ are defined by the acoustic medium parameters of the background medium (bg) and the object medium (obj) via

$$\Delta\hat{\eta}(\mathbf{x}') = \hat{s}(\kappa^{\text{bg}} - \kappa^{\text{obj}}(\mathbf{x}')), \tag{5}$$

$$\Delta\hat{\zeta}(\mathbf{x}') = \hat{s}(\rho^{\text{bg}} - \rho^{\text{obj}}(\mathbf{x}')), \tag{6}$$

while the Green's tensor operators applied to a volume density of injection rate source $\hat{q}(\mathbf{x})$ or a volume density of force $\hat{f}_j(\mathbf{x})$ read as follows:

$$\hat{G}^{pq}(\mathbf{x},\mathbf{x}')[q(\mathbf{x}')] = \hat{s}\rho^{\text{bg}}\hat{G}(\mathbf{x},\mathbf{x}') * q(\mathbf{x}'), \tag{7}$$

$$\hat{G}_j^{pf}(\mathbf{x},\mathbf{x}')[f_j(\mathbf{x}')] = -\partial_j\hat{G}(\mathbf{x},\mathbf{x}') * f_j(\mathbf{x}'), \tag{8}$$

$$\hat{G}_k^{vq}(\mathbf{x},\mathbf{x}')[q(\mathbf{x}')] = -\partial_k\hat{G}(\mathbf{x},\mathbf{x}') * q(\mathbf{x}'), \tag{9}$$

$$\hat{G}_{k,j}^{vf}(\mathbf{x},\mathbf{x}')[f_j(\mathbf{x}')] = \frac{1}{\hat{s}\rho^{\text{bg}}}[\partial_k\partial_j\hat{G}(\mathbf{x},\mathbf{x}') * f_j(\mathbf{x}') + \delta_{k,j}\delta(\mathbf{x}-\mathbf{x}') * f_j(\mathbf{x}')], \tag{10}$$

with ∂_k the partial derivative in the x_k direction, $\delta_{k,j}$ Kronecker's delta function, $\delta(\mathbf{x}-\mathbf{x}')$ the three-dimensional (3D) Dirac delta function and with $\hat{G}(\mathbf{x},\mathbf{x}')$ the scalar form of Green's function. Note that, $g(\mathbf{x},\mathbf{x}') * h(\mathbf{x}')$ defines a convolution over the spatial domain $\mathbb{D}$ containing the contrasts and the transducers. Hence, in the absence of any contrast, the acoustic wave field will travel with the speed of sound c,

$$c = \frac{1}{(\kappa^{\text{bg}}\rho^{\text{bg}})^{1/2}}, \tag{11}$$

through the medium.

This integral formulation is applied to the situation shown in Fig. 1. Here, an object is positioned in a homogeneous background medium, while around the object at equiangular positions β_m a set of transducers is positioned. In the mono-static situation, only one transducer is used which acts as both a transmitter and a receiver, hence $\mathbf{x}^{\text{src}} = \mathbf{x}^{\text{rec}}$. Multiple measurements are made by rotating the transducer around

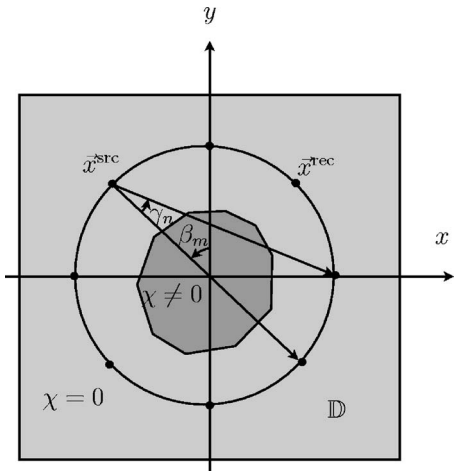

FIG. 1. The setup used for fan-beam measurements. A transmitter positioned at $\mathbf{x}^{\mathrm{src}}$ will create an acoustic wave field which is observed by the receivers located at $\mathbf{x}^{\mathrm{rec}}$.

the object, or vice-versa. For tomographic fan-beam measurements, a multi-static setup is used. Therefore, one transducer will act as a transmitter while the remainder act as receivers. Again, a complete set of measurements is obtained by rotating the transmitter and receivers around the object.

Equations (3) and (4) form an integral equation of the second type. After discretization, these equations are solved by using a conjugate gradient inversion scheme, as described by Refs. 36, 37, 39, and 40. The method includes a recursive procedure to compute the unknowns $\hat{p}^{\mathrm{tot}}(\mathbf{x})$ and $\hat{v}_k^{\mathrm{tot}}(\mathbf{x})$ with Polak-Ribière conjugate gradient update directions. The scheme is based on the minimization of the L_2-norm of an error functional. This error functional is defined as the difference between the known incident fields $\hat{p}^{\mathrm{inc}}(\mathbf{x})$ and $\hat{v}_k^{\mathrm{inc}}(\mathbf{x})$ and the approximated incident fields based on the computed scattered and total fields at the nth iteration step, $\hat{p}^{\mathrm{tot}}(\mathbf{x}) - \hat{p}^{\mathrm{sct}}(\mathbf{x})$ and $\hat{v}_k^{\mathrm{tot}}(\mathbf{x}) - \hat{v}_k^{\mathrm{sct}}(\mathbf{x})$. This method is usually referred to as the "conjugate gradient method applied to the normal equations."

III. INVERSE PROBLEM

The aim of imaging is to localize contrasts and to compute speed of sound profiles from which temperature distributions in the region of interest can be obtained. In this paper, three imaging methods are compared. The first imaging method is described well by Kak and Slaney[25] and is based on the Fourier slice theorem and uses changes in travel times as observed in tomographic fan-beam projection data. The second and third methods are based on the acoustic wave equations. In these cases, the Born approximation is used to find an approximate solution of an integral equation similar to the one used for the forward modeling. Both a single step and an iterative scheme are considered.

A. Fourier slice method

The fan-beam slice theorem[25] is based on optical ray theory, where only changes in time delays are taken into account. These time delays are related to changes in the medium parameters density and compressibility, while effects like attenuation and diffraction are neglected. Within these approximations, the direct problem is solved by computing the two-dimensional (2D) Radon transform,

$$P_\beta(\gamma_n) = \int_{(x,y)=-\infty}^{\infty} c^{-1}(x,y)\,\delta\left(x\cos\left(\frac{1}{2}\pi-\beta-\gamma\right) + y\sin\left(\frac{1}{2}\pi-\beta-\gamma\right) - R\sin(\gamma)\right)dxdy, \tag{12}$$

with R the radius of the circle defining the transducer positions, β the angle between the y axis and the transmitter, and γ_n the position of a ray in a fan-beam as shown in Fig. 1.

Using the formulation for the forward problem as given in Eq. (12), images are obtained in three steps. First the projection (Radon) data are multiplied by $R\cos(\gamma_n)$, hence

$$P'_{\beta_i}(\gamma_n) = P_\beta(\gamma_n) R\cos(\gamma_n). \tag{13}$$

Next, the modified projection data are filtered by convolving $P'_{\beta_i}(\gamma_n)$ with $g(\gamma_n)$,

$$Q_{\beta_i}(\gamma_n) = P'_\beta(\gamma_n) * g(\gamma_n), \tag{14}$$

where the filter function reads

$$g(\gamma_n) = \begin{cases} \dfrac{1}{8(\Delta\gamma)^2} & \text{when } n=0 \\ 0 & \text{when } n \text{ is even} \\ -\dfrac{1}{2}\left(\dfrac{1}{\pi\sin(\gamma_n)}\right)^2 & \text{when } n \text{ is odd.} \end{cases} \tag{15}$$

To improve the image quality, further filtering is often applied,

$$Q_{\beta_i}(\gamma_n) = P'_\beta(\gamma_n) * g(\gamma_n) * k(\gamma_n), \tag{16}$$

where $k(\gamma_n)$ is typically a cosine, Hamming, or Shepp-Logan filter. Finally, the amplitude of the reciprocal of the sound-speed profile is obtained by summing all the normalized filtered projections,

$$c^{-1}(x,y) = \Delta\beta\sum_{i=1}^{M} \frac{1}{|\mathbf{x}^{\mathrm{src}}(\beta_i)-(x,y)|^2} Q_{\beta_i}(\gamma'_n) \times \delta\left(x\cos\left(\frac{1}{2}\pi-\beta-\gamma\right) + y\sin\left(\frac{1}{2}\pi-\beta-\gamma\right) - R\sin(\gamma)\right), \tag{17}$$

where $|(x,y)|^2$ equals the L_2-norm of a vector. Note that the filter function $g(\gamma_n)$ shown in Eq. (15) is slightly different from that shown previously by Kak and Slaney[25] where $g(\gamma_n)$ reads

$$g(\gamma_n) = \left(\frac{1}{\pi\sin(\gamma_n)}\right)^2, \tag{18}$$

when n is odd, and was obtained after a thorough analysis of the original work presented in Ref. 25.

B. Backpropagation and conjugate gradient technique

The second group of reconstruction methods is based on the acoustic wave equation formulation used for the forward problem. Starting with Eq. (3) and assuming that there is only contrast in compressibility ($\Delta\hat{\zeta}(\mathbf{x})=0$) and that the problem is defined within the Born approximation, results in an approximation of the scattered pressure field which reads

$$\hat{p}^{\mathrm{sct}}(\mathbf{x}) = \hat{G}^{pq}(\mathbf{x},\mathbf{x}')\hat{s}\chi(\mathbf{x}')\hat{p}^{\mathrm{inc}}(\mathbf{x}'). \tag{19}$$

An estimate for $\chi(\mathbf{x}')$ is retrieved from a minimum norm solution of the error functional Err, where Err reads

$$\mathrm{Err} = \sum_{s,r,\omega} |\hat{p}^{\mathrm{sct}}(\mathbf{x}) - \hat{G}^{pq}(\mathbf{x},\mathbf{x}')\hat{s}\chi(\mathbf{x}')\hat{p}^{\mathrm{inc}}(\mathbf{x}')|^2, \tag{20}$$

with the subscripts s and r referring to a summation over all possible source and receiver positions. Minimization of the error functional Err in a single step is in literature referred to as backpropagation. With backpropagation, we approximate $\chi(\mathbf{x}')$ by

$$\chi(\mathbf{x}') = \alpha\Delta\chi(\mathbf{x}'), \tag{21}$$

where α is a real constant. The error functional Err in Eq. (20) tends toward a minimum when α reads

$$\alpha = \frac{\Re\left(\sum_{s,r,\omega} \hat{G}^{pq}(\mathbf{x},\mathbf{x}')\hat{s}\Delta\chi(\mathbf{x}')\hat{p}^{\mathrm{inc}}(\mathbf{x}')[\hat{p}^{\mathrm{sct}}(\mathbf{x}')]^*\right)}{\sum_{s,r,\omega} |\hat{G}^{pq}(\mathbf{x},\mathbf{x}')\hat{s}\Delta\chi(\mathbf{x}')\hat{p}^{\mathrm{inc}}(\mathbf{x}')|^2}, \tag{22}$$

where $\Re(\ldots)$ is used to denote that the real part is taken. We observe that, apart from a constant, the numerator is maximized by taking as update direction

$$\Delta\chi(\mathbf{x}') = \sum_{s,r,\omega} (\hat{p}^{\mathrm{inc}}(\mathbf{x}')\hat{s}^2\rho\hat{G}(\mathbf{x},\mathbf{x}'))^*\hat{p}^{\mathrm{sct}}(\mathbf{x})\Delta V, \tag{23}$$

with ΔV the size of a volume element and where $(\ldots)^*$ is used to denote that the complex conjugate of the operator is taken. Substituting this in Eq. (22) we obtain for α,

$$\alpha = \frac{\sum_{s,r,\omega} \hat{p}^{\mathrm{sct}}(\mathbf{x}')[\hat{p}^{\mathrm{sct}}(\mathbf{x}')]^*}{\sum_{s,r,\omega} |\hat{p}^{\mathrm{sct}}(\mathbf{x}')|^2}. \tag{24}$$

Backpropagation is similar to the first step in a CG inversion scheme. With the CG method, the set of equations present in Eq. (19) is solved iteratively by minimizing the error functional Err in Eq. (20).[36,37]

Since the Fourier method is a 2D reconstruction method, the computation of $\Delta\chi(\mathbf{x}')$ is restricted to the plane containing the transducers. Finally, a speed of sound profile is obtained from the computed contrast profile via

$$c(\mathbf{x}) = \left(\frac{1}{|\kappa^{\mathrm{bg}} - \Re(\chi)|\rho^{\mathrm{bg}}}\right)^{1/2}, \tag{25}$$

where it is assumed that changes in the density are compensated for by changes in the compressibility. This is based on the observation that the scattered pressure field is partly caused by the velocity field via changes in density, see the second term on the right-hand side of Eq. (3). However, this term is neglected in Eq. (19) and will be compensated via additional changes in the compressibility.

TABLE I. The medium parameters compressibility, κ, volume density of mass, ρ, and speed of sound, c, for various tissues.

	Compressibility $k[10^{-9}(\mathrm{Pa})^{-1}]$	Density $\rho[\mathrm{kg/m^3}]$	Speed of sound $c[\mathrm{m/s}]$
Liver at 37 °C	0.366 48	1056.6	1607
Liver at 45 °C	0.105 33	1053.3	1612
Liver at 50 °C	0.365 71	1051.0	1613
Fat	0.481 9	950.0	1478

IV. RESULTS AND DISCUSSION

Synthetic data for three different configurations was computed by solving Eqs. (3) and (4) in the frequency domain and transforming the obtained results into time domain using fast Fourier transforms (FFTs). In all cases, a homogeneous background medium was used with acoustic medium parameters similar to liver, in order that a good impression of the accuracy of the methods employed could be obtained. In practice, the background medium is unlikely to be homogeneous, but the techniques employed may also use an inhomogeneous background medium provided that its profile is known in advance of any heating, i.e., the changes in the starting profile are related to the changes in temperature. Various contrasts were present in the homogeneous background medium used in this simulation, representing regions of either fat or heated liver tissue. The corresponding medium parameters are shown in Table I and were obtained by combining the results presented by Refs. 14, 15, and 23. Note that the changes in speed of sound due to heating are relatively small, viz. 5 m/s between 37 and 45 °C and 1 m/s between 45 and 50 °C. The three-dimensional (3D) volume under investigation contained $64\times64\times8$ elements of size $2.5\times2.5\times2.5$ mm^3. Each real valued temporal signal contained 256 points, with 1.56 μs temporal step size. All acoustic sources were defined via a real valued volume density of injection rate with amplitude equal to one in the temporal Laplace domain.

Typical results for the incident, scattered, and total pressure wave fields for a configuration containing two heated regions are shown in Fig. 2. The heated regions form a known semi-infinite 3D contrast profile of which a cross section is shown in Fig. 2(a). The results show that the amplitude of the scattered wave field is one order of magnitude lower than the magnitude of the incident wave field. Consequently, the presence of the objects is hardly visible in the total wave field, despite the fact that all spatial dimensions of all the objects are bigger than the smallest wavelength present in the probing signal.

Projection data were obtained by computing the total wave fields for 36 transmitter positions marked by an open circle in Fig. 3(a). Next, standard cross correlation was used to compute the time delays between the incident and the total pressure wave fields at the remaining receiver positions. To

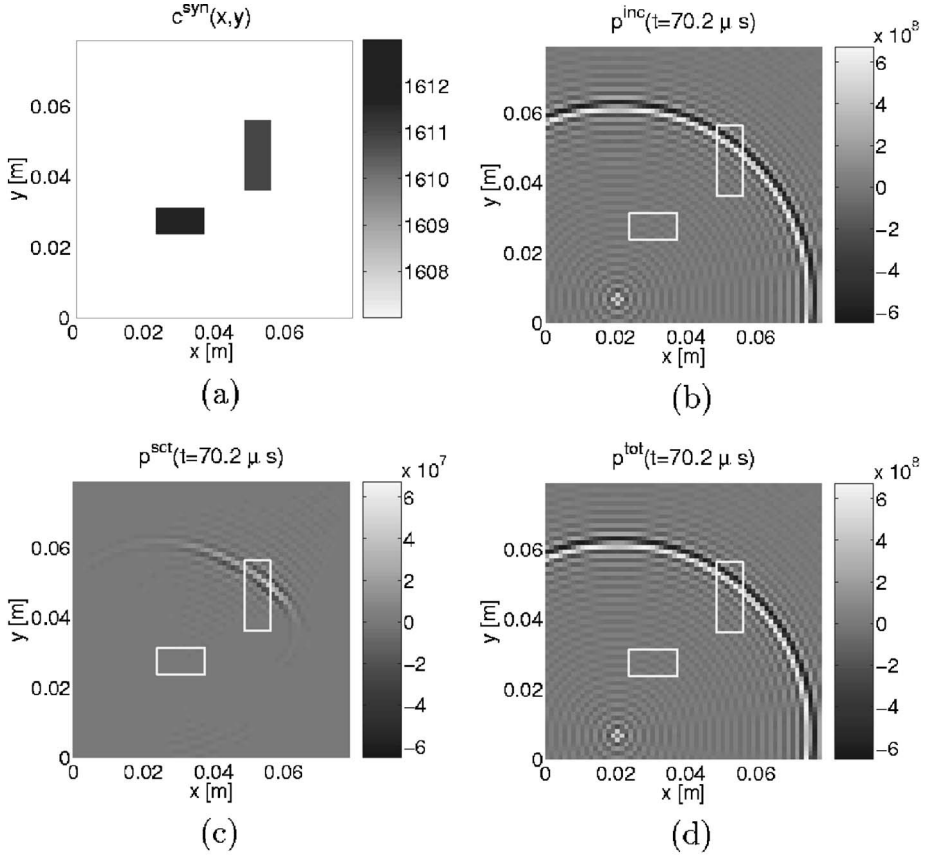

FIG. 2. Due to the presence of various contrasts (a), the incident wave field (b)generates a scattered field (c), which combined results in the total wave field (d). The boxes represent the location of the objects.

increase the temporal resolution, cubic spline interpolation was applied to both time domain signals to increase the number of samples by a factor of 1000. An example for the result obtained with cross correlation applied to the signals shown in Fig. 3(b) is given in Fig. 3(c), showing a time delay of 11 ns. The signals were obtained from the transmitter-receiver combination indicated by the line in Fig. 3(a). Repeating this procedure for all transmitter-receiver combinations resulted in the Radon transform shown in Fig. 4(a). For the same configuration the (ideal) Radon transform was also computed within the optical ray approximation using Eq. (12). The obtained results are shown in Fig. 4(b). Comparing the results, it is observed that the images show similar patterns, but with different amplitudes. Hence, time delays are observed for the same transmitter-receiver combinations, but with smaller time delays for the full solution. This is mainly due to diffraction which is not taken into account in the optical ray approximation.

Projection data as shown in Fig. 4 were used as input data for the Fourier slice algorithm. It is found that the image quality improves by correcting the projection data before processing for the background medium, i.e., when changes in a known starting background profile are being imaged. Hence, the projection $P_\beta(\gamma_n)$ used for the imaging reads

$$P_\beta(\gamma_n) = P_\beta^{\text{meas}}(\gamma_n) - P_\beta^{\text{bg}}(\gamma_n), \tag{26}$$

with $P_\beta^{\text{meas}}(\gamma_n)$ the measured projection and $P_\beta^{\text{bg}}(\gamma_n)$ the projection computed in the absence of any objects based on the known background medium parameters.

In total, three different configurations were used for testing the imaging algorithms. In the first configuration, two regions are present which are different in size and have different sound-speeds. A cross section of the sound-speed profile is shown in Fig. 5(a) while the corresponding Radon transforms are given in Fig. 4. Results with the Fourier method based on data within the optical ray approximation are shown in Fig. 5(b) and show that the regions are clearly present in the reconstructed sound-speed profiles with correct magnitudes. It is found that by increasing the number of measurements and decreasing the grid size the high amplitude noise at the edge of the image near the transducers will decrease and that sharper edges defining the regions will be obtained. However, the optical ray approximation effectively ignores diffraction. Next, the same Fourier method was used on Radon data based on the full solution of the forward problem. The reconstructed speed of sound profile from this data is shown in Fig. 5(c) and shows that both regions are localized. However, comparing these results with the reconstructions from data obtained via the line integrals shows that the region boundaries have become more blurred and that the reconstructed sound-speeds have decreased. This is in accordance with the results shown in Fig. 4, where the amplitude of the Radon data based on a full solution of the forward problem is smaller than the amplitude of the Radon data based on the line integral. Note that the region with the smallest spatial dimension but with the highest speed of

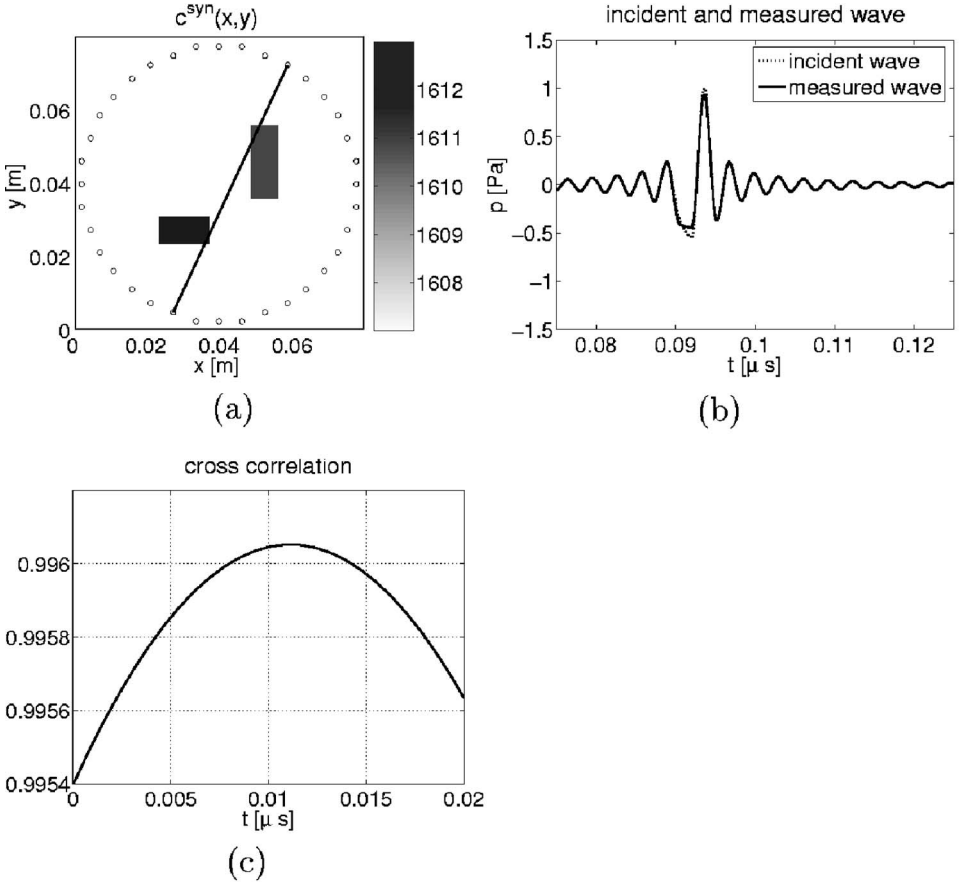

FIG. 3. For one transmitter-receiver combination, indicated by the line in (a), the incident and measured waves are obtained (b). Standard cross correlation is used to compute the time delay for this transducer combination (c).

sound has the lowest sound-speed in the reconstructed image. Next, we transformed the time domain data based on the full solution of the forward problem back to the frequency domain. Hence, each real valued temporal signal resulted in 127 complex valued data points in the frequency domain where we omitted the zero and highest frequency component of the signal. This corresponds to acoustic frequencies from 2.5 up to 320.5 kHz. On this frequency domain data set we first applied backpropagation where we used all frequency components. The resulting image is shown in Fig. 5(d). With this method the regions are localized and less blurred when compared to the results obtained with the Fourier method. However, the amplitudes of the reconstructed sound-speed profiles are lower than in the original profiles. The results improve by using the conjugate gradient method on the same complex valued frequency domain data. After only three iterations, the edges have become sharper and the magnitudes of the reconstructed velocities are higher as can be observed from Fig. 5(e). Due to the roughness in amplitudes of the reconstructed heated regions the error in some individual elements can be as high 2 m/s, therefore, the amplitude is clipped at some locations in the image. More iterations do not improve the image.

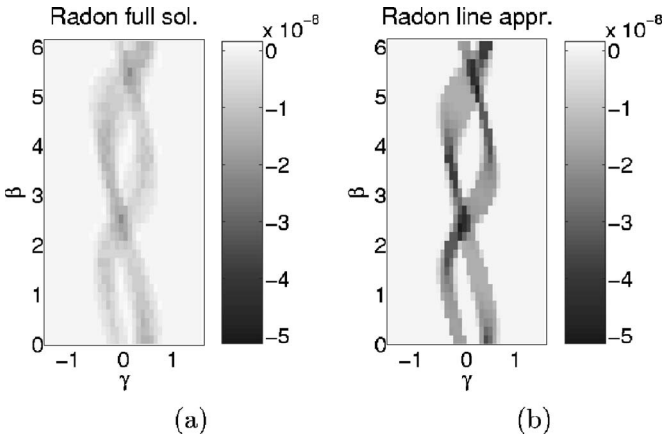

FIG. 4. The Radon transformation based on (a) the full solution of the forward problem and on (b) optical ray theory.

From the above-presented results, it is observed that the size of a region influences the amplitude of the reconstructed image in the case where data based on the full solution of the forward problem are used. In order to verify this observation, a configuration was taken where there are three regions with different spatial dimensions but identical sound-speeds (all regions represent tissue heated to 50 °C). Applying the same computational schemes resulted in the contrast profiles shown in Fig. 6. The results show that with the Fourier method and the full solution data, the smallest region is not localized, while with the backpropagation and conjugate gradient method it is localized successfully. It also shows that the amplitude of the reconstructed sound-speed profiles indeed depend on the size of the region. These results suggest that, with the CG method, smaller regions can be detected than with the Fourier method. Consequently, a third configuration has been considered where there is a small region of the same dimension with high acoustic contrast, i.e., a small region of fat. The results for this configuration are shown in Fig. 7. In this case, only the Fourier method is capable of

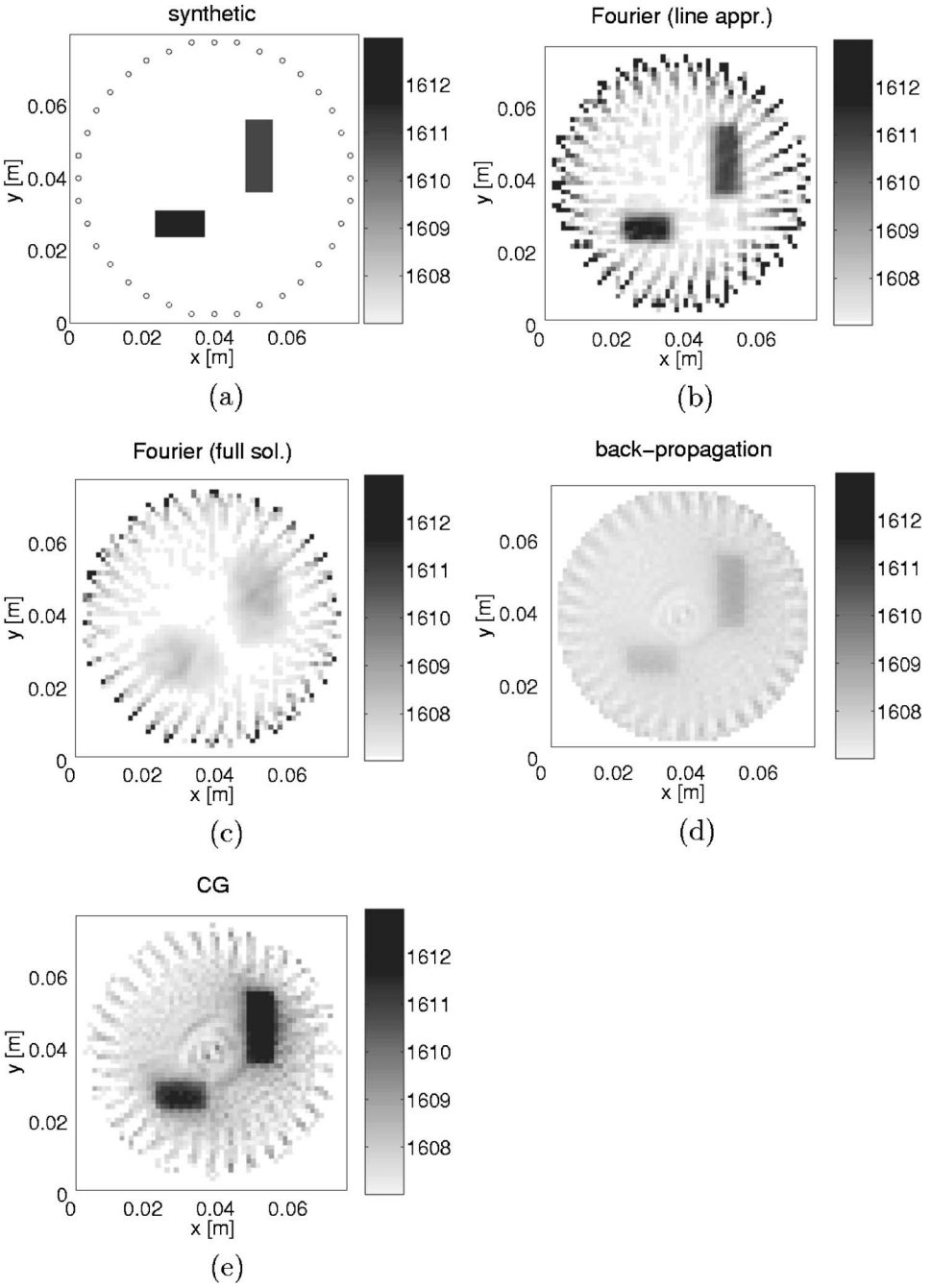

FIG. 5. The cross section (a) of a semi-infinite 3D known contrast function based on two different heated regions. Next, two images are shown with results obtained by applying the Fourier technique on synthetic data (b) computed via line integrals and (c) computed by solving the full vectorial forward problem. The results improve when (d) backpropagation or an (e) conjugate gradient scheme is applied.

localizing the region of fat, while the remaining two heated regions disappear in the background noise. With the backpropagation and conjugate gradient method, none of the regions are localized due to the noise present in the image. This noise is caused by the combination of the high frequency content of the signal and the high contrast of the fat. This problem is solved by using the first 32 frequencies (i.e., up to 20 kHz) of the signal at the expense of the obtained spatial resolution. Hence, the location of the fat region becomes clear in the backpropagation image, while the reconstruction obtained with the CG method also reveals the location of the heated regions after applying 32 iterations. The reconstructed speeds of sound in the regions are higher than the expected values due to the presence of the high contrast of the fat region. The images are expected to improve if this contrast is taken into account in the initial background profile, as such a high contrast would already be observed prior to heating.

In order to demonstrate the capabilities of the imaging methods we have chosen contrasts with sharp edges. In reality a heated region would have smooth edges and a Gaussian temperature distribution. If this is taken into account during reconstruction it would result in a decrease of the noise in the distribution and therefore a further increase of the accuracy of the reconstruction.

Finally, it should be noted that the Fourier method has the advantage over the backpropagation or CG method of being relatively easy to implement; as the algorithm is less complex and the required Radon data are easier to obtain by applying simple cross-correlation techniques on measured

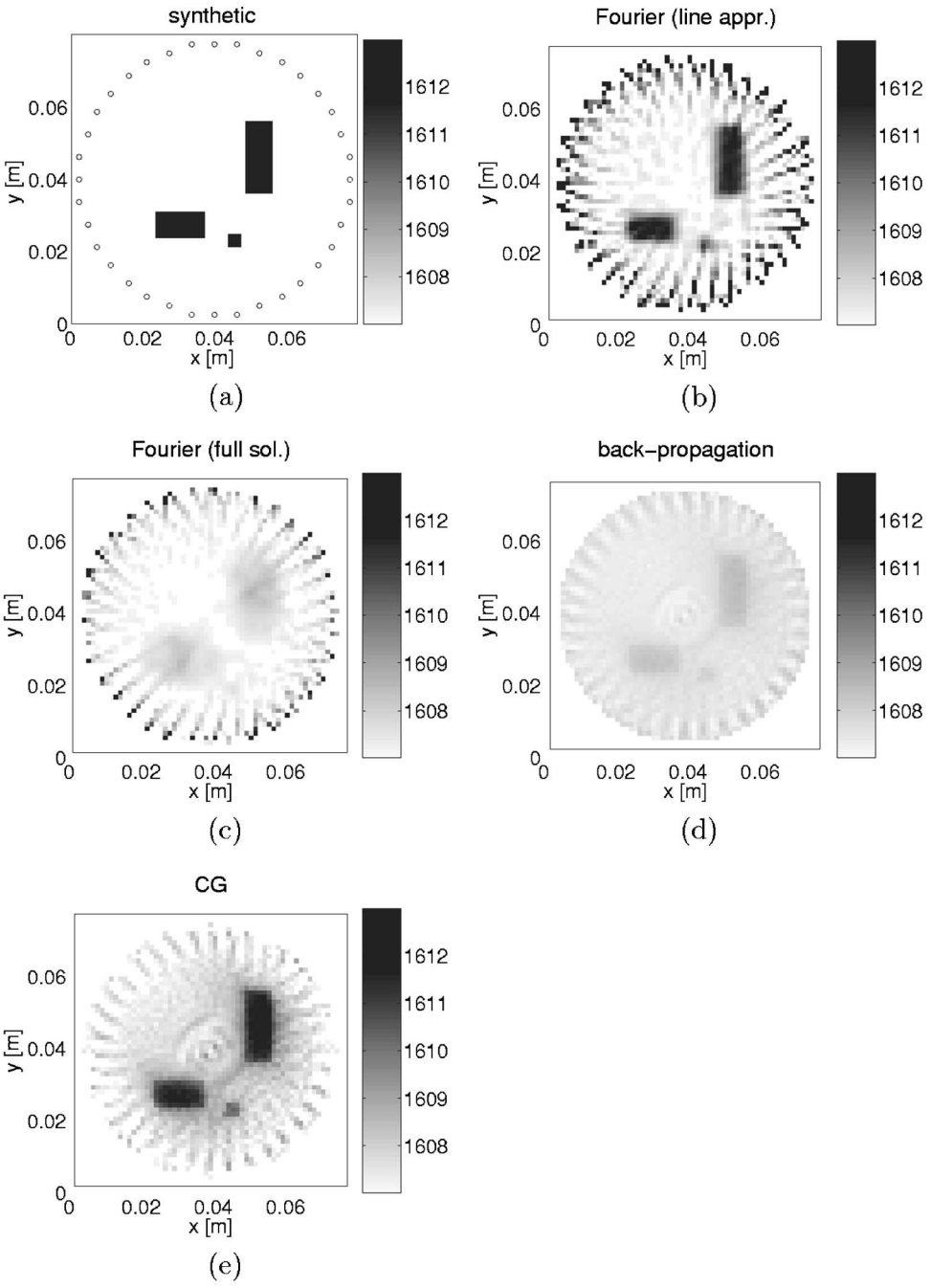

FIG. 6. The cross section (a) of a semi-infinite 3D known contrast function based on three heated regions. Next, two images are shown with results obtained by applying the Fourier technique on synthetic data (b) computed via line integrals and (c) computed by solving the full vectorial forward problem. The results improve when (d) backpropagation or an (e) conjugate gradient scheme is applied.

tomographic data. In addition, the Fourier method has the advantage of being computationally less expensive than the backpropagation or the CG method.

V. CONCLUSION

The feasibility of using low frequency (2.5–320 kHz) ultrasound to image the weakly scattering contrasts expected during HIFU treatment has been investigated. Representative imaging algorithms from two groups of imaging methods have been compared and tested on the same synthetic data set. Both groups are usually used independently and have not been compared directly. The first group uses Radon or projection data to compute 2D sound-speed profiles of the volume of interest. The reconstruction methods rely on optical ray theory and the Fourier slice technique was taken as a representative example from this group of imaging methods. The second group uses the acoustic wave equations as starting point. A backpropagation and a conjugate gradient inversion scheme were considered, both defined within the Born approximation. All schemes were restricted to the 2D situation.

Three configurations were used to test the imaging methods on (weakly) scattering contrasts which typically occur during hyperthermia cancer treatment. In all cases, the contrasts represented regions of fat or heated tissue which are embedded in a homogeneous background medium with acoustic medium properties equivalent to that of human liver at 37 °C. Synthetic data were computed by solving the complete vectorial forward problem for both the pressure and velocity wave fields, taking changes in compressibility and volume density of mass into account. Only the pressure wave fields were used for imaging.

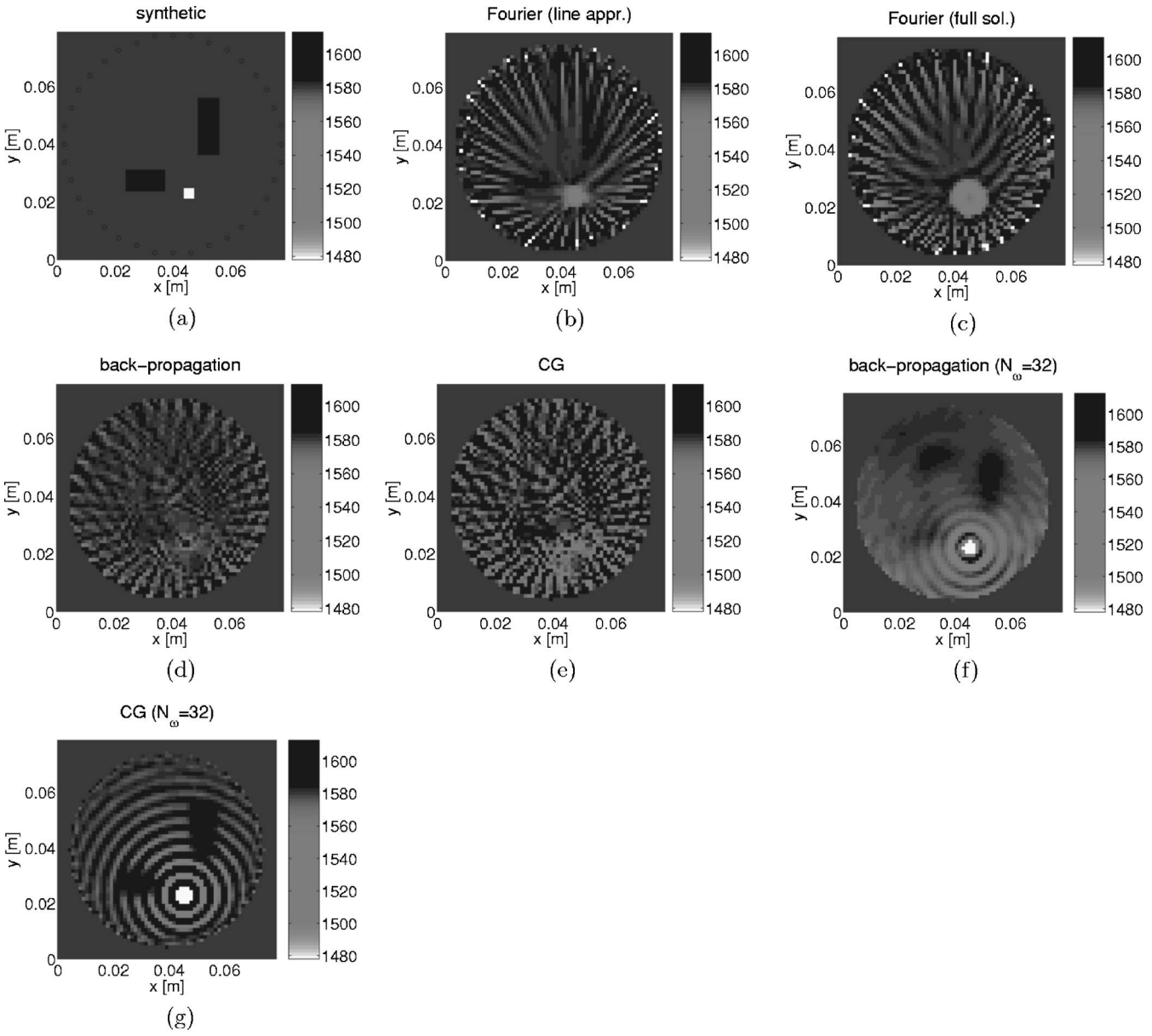

FIG. 7. The cross section (a) of a semi-infinite 3D known contrast function based on two different heated regions and one fat region. Next, two images are shown with results obtained by applying the Fourier technique on synthetic data (b) computed via line integrals and (c) computed by solving the full vectorial forward problem. The results obtained with backpropagation and a conjugate gradient scheme are shown in (d)–(g).

The results obtained show that all methods could detect changes in speed of sound due to an increase in temperature. Poor spatial resolution of the object was obtained with the Fourier method. In addition, the amplitudes of the reconstructed speed of sound profiles were lower than their synthetic values. To compare, in the situation where there was only one type of contrast, with an increase in speed of sound at the object location from 1607 to 1613 m/s the reconstructed profile showed only an increase up to 1609 m/s. With the backpropagation method comparable results were obtained for the amplitudes of the reconstructed sound-speed profiles. However, the results showed an increase in spatial resolution. With the conjugate gradient method the spatial resolution improved even further, while the reconstructed sound-speed values became too high; for the same configuration the increase was up to 1614 m/s.

Increases in temperature for regions as small as the shortest wavelength present in the probing signal were only detected with the backpropagation and conjugate gradient methods. In the situation where the same small object was a small region of fat with high acoustic contrast, the Fourier method was capable of localizing the fat region but not the heated regions. Both the backpropagation and the CG method could reveal the location of the fat region after removing the highest frequencies present in the measured signal, while of all methods only the CG method could reveal the locations of the heated regions.

The work has demonstrated that it is feasible to use low frequency ultrasound to image the small weakly scattering acoustic contrasts that would be expected to occur during hyperthermia cancer treatment, and that a good accuracy is obtained when using the CG reconstruction method.

ACKNOWLEDGMENTS

This work was supported by Marie Curie Intra-European Fellowship No. MEIF-CT-2003-501333. The authors also gratefully acknowledge all the fruitful discussions they had with K. M. Bograchev. Finally, they would like to thank the Boole Centre for Research in Informatics, University College Cork, Ireland, for the usage of their computer facility.

[1]S. J. Norton and M. Linzer, "Ultrasonic reflectivity imaging in three dimensions: Exact inverse scattering solutions for plane, cylindrical and spherical apertures," IEEE Trans. Biomed. Eng. **28**(2), 202–220 (1981).
[2]J. F. Greenleaf and R. C. Bahn, "Clinical imaging with transmissive ultrasonic computerized-tomography," IEEE Trans. Biomed. Eng. **28**(2), 177–185 (1981).
[3]A. J. Devaney, "A filtered back-propagation algorithm for diffraction tomography," Ultrason. Imaging **4**(4), 336–350 (1982).
[4]S. A. Johnson, D. A. Christensen, C. C. Johnson, J. F. Greenleaf, and B. Rajagopalan, "Nonintrusive measurement of microwave or ultrasound induced hyperthermia by acoustic temperature tomography," Proc.-IEEE Ultrason. Symp. 977–982 (1977).
[5]N. T. Sanghvi, F. J. Fry, R. Bihrle, R. S. Foster, M. H. Phillips, J. Syrus, A. V. Zaitsev, and C. W. Hennige, "Noninvasive surgery of prostate tissue by high-intensity focused ultrasound," IEEE Trans. Ultrason. Ferroelectr. Freq. Control **43**, 1099–1110 (1996).
[6]J. E. Kennedy, G. R. ter Haar, and D. Cranston, "High intensity focused ultrasound: Surgery of the future," Br. J. Radiol. **76**, 590–599 (2003).
[7]G. Ter Haar, "Ultrasound focal beam surgery," Ultrasound Med. Biol. **21**, 1089–1100 (1995).
[8]C. J. Diederich and K. Hynynen, "Ultrasound technology for hyperthermia," Ultrasound Med. Biol. **25**, 871–887 (1999).
[9]K. A. Wear, R. F. Wagner, M. F. Insana, and T. J. Hall, "Application of autoregressive spectral analysis to cepstral estimation of mean scatterer spacing," IEEE Trans. Ultrason. Ferroelectr. Freq. Control **40**, 50–58 (1993).
[10]N. T. Sanghvi, R. S. Foster, F. J. Fry, R. Bihrle, C. Hennige, and L. V. Hennige, "Ultrasound intracavity system for imaging, therapy planning and treatment of focal disease," Proc.-IEEE Ultrason. Symp. **2**, 1249–1253 (1992).
[11]R. Seip, P. VanBaren, and E. S. Ebbini, "Dynamic focusing in ultrasound hyperthermia treatments using implantable hydrophone arrays," IEEE Trans. Ultrason. Ferroelectr. Freq. Control **41**, 706–713 (1994).
[12]R. Seip and E. S. Ebbini, "Noninvasive estimation of tissue temperature response to heating fields using diagnostic ultrasound," IEEE Trans. Biomed. Eng. **42**, 828–839 (1995).
[13]A. N. Amini, E. S. Ebbini, and T. T. Georgiou, "Noninvasive estimation of tissue temperature via high-resolution spectral analysis techniques," IEEE Trans. Biomed. Eng. **52**(2), 221–228 (2005).
[14]N. R. Miller, J. C. Bamber, and G. R. ter Haar, "Imaging of temperature-induced echo strain: Preliminary in vitro study to assess feasibility for guiding focused ultrasound surgery," Ultrasound Med. Biol. **30**(3), 345–356 (2004).
[15]R. Souchon, G. Bouchoux, E. Maciejko, C. Lafon, D. Cathignol, M. Bertrand, and J. Y. Chapelon, "Monitoring the formation of thermal lesions with heat-induced echo-strain imaging: A feasibility study," Ultrasound Med. Biol. **31**(2), 251–259 (2005).
[16]N. R. Miller, J. C. Bamber, and P. M. Meaney, "Fundamental limitations of noninvasive temperature imaging by means of ultrasound echo strain estimation," Ultrasound Med. Biol. **28**(10), 1319–1333 (2002).
[17]J.-W. Jeong, T.-S. Kim, D. C. Shin, S. Do, M. Singh, and V. Z. Marmarelis, "Soft tissue differentiation using multiband signatures of high resolution ultrasonic transmission tomography," IEEE Trans. Med. Imaging **24**(3), 399–408 (2005).
[18]Y. Nawata and K. Kaneko, "Measurement of temperature distribution in phantom body by an ultrasonic CT method," Proceedings of the ASME/JSME Joint Thermal Engineering Conference 1999, Vol. **3**, pp. 469–474.
[19]D. Kourtiche, M. Nadim, G. Kontaxakis, C. Marchal, and G. Prieur, "Temperature measurements using US tomography: Theoretical aspects," Proc. IEEE Eng. Med. Biol. Soc. **13**(1), 325–326 (1991).
[20]P. Lasaygues and J. P. Lefebvre, "Cancellous and cortical bone imaging by reflected tomography," Ultrason. Imaging **23**(1), 55–70 (2001).
[21]M. Muller, P. Moilanen, E. Bossy, P. Nicholson, V. Kilappa, T. Timonen, M. Talmant, S. Cheng, and P. Laugier, "Comparison of three ultrasonic axial transmission methods for bone assessment," Ultrasound Med. Biol. **31**(5), 633–642 (2005).
[22]T. Miyashita, "Low-frequency scattering component for quantitative circular-scanning ultrasonic diffraction tomography," Jpn. J. Appl. Phys., Part 1 **40**(5B), 3926–3930 (2001).
[23]T. D. Mast, "Empirical relationships between acoustic parameters in human soft tissues," ARLO **1**, 37–42 (2000), and references herein.
[24]A. J. Devaney and M. Dennison, "Inverse scattering in inhomogeneous background media," Inverse Probl. Eng. **19**(4), 855–870 (2003).
[25]A. T. Kak and M. Slaney, *Principles of Computerized Tomographic Imaging* (IEEE, New York, 1988).
[26]K. M. Bograchev and W. M. D. Wright, "Computer modelling of iterative technique application for tissue thermal imaging," Proc.-IEEE Ultrason. Symp. **21**, 2038–2041 (2005).
[27]N. V. Ruiter, M. Zapf, R. Stotzka, T. O. Muller, K. SchloteHolubek, G. Göbel, and H. Gemmeke, "First images with a 3d prototype for ultrasound computer tomography," Proc.-IEEE Ultrason. Symp. **21**, 2042–2045 (2005).
[28]R. A. Crowther, D. J. Derosier, and A. Klug, "The reconstruction of a three-dimensional structure from projections and its application to electron microscopy," Proc. R. Soc. London, Ser. A **317**, 319–340 (1970).
[29]A. Abubakar, T. M. Habashy, P. M. van den Berg, and D. Gisolf, "The diagonalized contrast source approach: An inversion method beyond the Born approximation," Inverse Probl. Eng. **21**, 685–702 (2005).
[30]M. Dobroka, L. Dresen, C. Gelbke, and H. Ruter, "Tomographic inversion of normalized data-double-trace tomography algorithms," Geophys. Prospect. **40**(1), 1–14 (1992).
[31]J. A. Scales, "Tomographic inversion via the conjugate gradient method," Geophysics **52**(2), 179–185 (1987).
[32]M. M. Bronstein, A. M. Bronstein, M. Zibulevsky, and H. Azhari, "Reconstruction in diffraction ultrasound tomography using nonuniform FFT," IEEE Trans. Med. Imaging **21**, 1395–1401 (2002).
[33]A. J. Davies, *The Finite Element Method- A First Approach* (Clarendon, Oxford, 1980).
[34]A. Taflove, *Computational Electrodynamics: The Finite-Difference Time-Domain Method* (Artech House, Norwood, MA, 1995).
[35]J. W. Daniel, "The conjugate gradient method for linear and nonlinear operator equations," SIAM (Soc. Ind. Appl. Math.) J. Numer. Anal. **4**, 10–26 (1967).
[36]R. E. Kleinman and P. M. van den Berg, "Iterative methods for solving integral equations," *PIERS 5, Application of Conjugate Gradient Method to Electromagnetics and Signal Analysis*, edited by T. K. Sarkar (Elsevier, New York, 1991), pp. 67–102.
[37]P. M. van den Berg, "Iterative schemes based on minimization of a uniform error criterion," in Ref. 36, pp. 27–66.
[38]A. T. de Hoop, *Handbook of Radiation and Scattering of Waves: Acoustic Waves in Fluids, Elastic Waves in Solids, Electromagnetic Waves* (Academic, London, 1995).
[39]K. W. A. van Dongen, C. Brennan, and W. M. D. Wright, "A reduced forward operator for acoustic scattering problems," Proceedings of the IEE Irish Signals and Systems Conference, Dublin, Ireland, 1–2 September 2005, pp. 294–299.
[40]A. F. Peterson, S. L. Ray, and R. Mittra, *Computational Methods for Electromagnetics* (Wiley-IEEE, New York, 1998).